Optimized Designs of Composite Booms with Integral Tape-Spring Hinges

H.M.Y.C. Mallikarachchi*

University of Cambridge, Cambridge CB2 1PZ, U.K.

S. Pellegrino†

California Institute of Technology, Pasadena, CA 91125

This paper presents an optimization study of a lightweight hinge consisting of a thin walled tube made of carbon fiber reinforced plastic with two longitudinal slots. The slot geometry is parameterized in terms of slot length, width and end circle diameter. Previously developed numerical simulation techniques to analyze the folding and deployment of this kind of hinges are used to carry out a series of parametric studies. The maximum strains are estimated by using the mid-surface strain and curvature obtained from a macro model of the structure to a micro model and averaging the strains over a half a tow width in the micro model. A maximum strain failure criterion is used for failure analysis. The optimization study is focused on finding a hinge design that can be folded 180 deg with the shortest possible slot length. Simulations show that the maximum strains can be significantly reduced by allowing the end cross-sections to deform freely. Based on simulations a failure critical model and a failure safe model were selected and experimentally validated. The optimized design is six times stiffer in torsion, twice stiffer axially and stores two and a half times more strain energy than the previously considered design.

I. Introduction and Background

Stored energy deployable structures made of composite materials have several advantages over traditional deployable structures with mechanical joints. Their lightness, lower cost due to a smaller number of components, and behavior insensitive to friction are distinctive advantages. Structures based on this approach have already been used in a few missions and a range of novel structural architectures that exploit this approach in future missions has been proposed. For example, Astro Aerospace Flattenable Foldable Tubes (FFT) were used as deployable antennas on MARSIS,[1] and RUAG's self-motorized deployment mechanism[2] and DLR's lightweight deployable booms[3] are examples of recent technology developments for future missions.

We are doing research on this kind of structures, with focus on a self-deployable hinge that is made by cutting longitudinal slots in a lightweight, thin-walled composite tube. The slots leave two continuous strips of material (tape springs) connecting the two ends of the tube, and these tape springs can be folded elastically to rotate one end of the tube with respect to the other end. The whole assembly is known as a tape-spring hinge.[4] We have published studies of the quasi-static and dynamic deployment behavior of a particular tape-spring hinge[5–7] made of two-ply ± 45 plain weave carbon fiber reinforced polymer (CFRP) material. The focus of the present paper is to use the simulation tools from our previous research to arrive at optimized designs for the geometry of the hinge. The material of the hinge is also being optimized, for example by varying the type of fabric, e.g. plain weave or triaxial weave, the number of plies and the ply arrangement, but in this paper we will focus on the hinge geometry.

Previous studies[6,7] have shown that the highest strains in the folded configuration occur near the ends of the slots. It was also found that in the hinge design considered previously the fold region in each tape spring

*Research Student, Department of Engineering, Trumpington Street, Cambridge CB2 1PZ, U.K. Currently on leave at California Institute of Technology

†Joyce and Kent Kresa Professor of Aeronautics and Professor of Civil Engineering, Graduate Aerospace Laboratories, 1200 E. California Blvd. MC 301-46. AIAA Fellow. sergiop@caltech.edu

could be moved along the length of the tape spring, suggesting that the length of the tape springs could possibly be shortened. Since there would be definite advantages in a more compact hinge design where a smaller amount of material is removed and so the slots are shorter and/or narrower, we have chosen the basic configuration shown in Figure 1 and explored what happens if we vary three parameters: the slot length, L, the slot width, SW, and the diameter of the end circles, D. These three parameters define the dimensions of a solid that extrudes the slot from a cylindrical tube.

In this paper we consider tubes with an internal diameter of 38 mm, thickness of 0.2 mm and areal density of 260 g/m^2. Initial values for the three parameters, L=60 mm, SW=10 mm and D=15 mm, were chosen based on Astro Aerospace FFT, which however is made from different materials. Our target is to obtain a tube hinge that can be safely folded 180 deg, and which requires only a minimum amount of material to be removed from the initial tube.

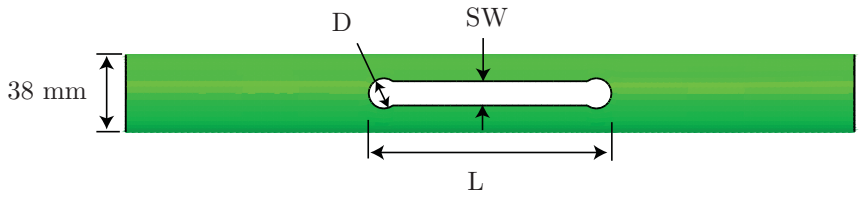

Figure 1: Hinge geometry.

II. Numerical Simulations

We use the commercial finite element software ABAQUS/Explict[8] for our simulations. Explicit time integration is conditionally stable and hence we keep all time increments below the critical value given by

$$\Delta t = \left(\sqrt{1+\xi^2} - \xi\right) \frac{l_{min}}{c_d} \tag{1}$$

where ξ = critical damping factor, l_{min} = minimum element length and $c_d \approx \sqrt{\frac{E}{\rho}}$ is the dilatational wave speed. Here E = elastic modulus and ρ = density.

A velocity-dependent normal viscous pressure is applied over all shell elements

$$p = -\, c_v \boldsymbol{v} \cdot \boldsymbol{n} \tag{2}$$

where c_v = viscous pressure coefficient, $\mathbf{v}$ = velocity and $\mathbf{n}$ = unit surface normal.

In addition we require that energy be conserved, to avoid numerical instabilities,[9] and check for this by monitoring that the energy balance (defined as the summation of internal energy, kinetic energy and viscous dissipation minus work done by the external forces) during each simulation is approximately zero throughout the simulation. More details are provided in Mallikarachchi and Pellegrino.[7]

Lastly, quasi-static behavior is maintained by ensuring that the kinetic energy to internal energy ratio be less than 1% and that there is zero kinetic energy in the fully folded configuration, at the end of a folding simulation.

A. Finite Element Model

In order to minimize the computational cost of this study, we have considered 180 mm long tube hinges, thus neglecting the effects of the structure to which the tube hinge would be connected in a real application. The tube hinge is modeled with four node fully integrated shell elements, S4, with an approximate length of 2 mm. The hinge is folded by specifying a rotation about the X-axis, Figure 2, of all the nodes lying on a 5 mm long strip at each end of the hinge. Apart from this imposed rotation, the end cross-sections of the tube hinge are allowed to deform freely and the only additional constraints that are imposed, to prevent rigid

body motion, are that two pairs of nodes of the end cross-sections are constrained in the X and Y-directions as shown in Figure 2.

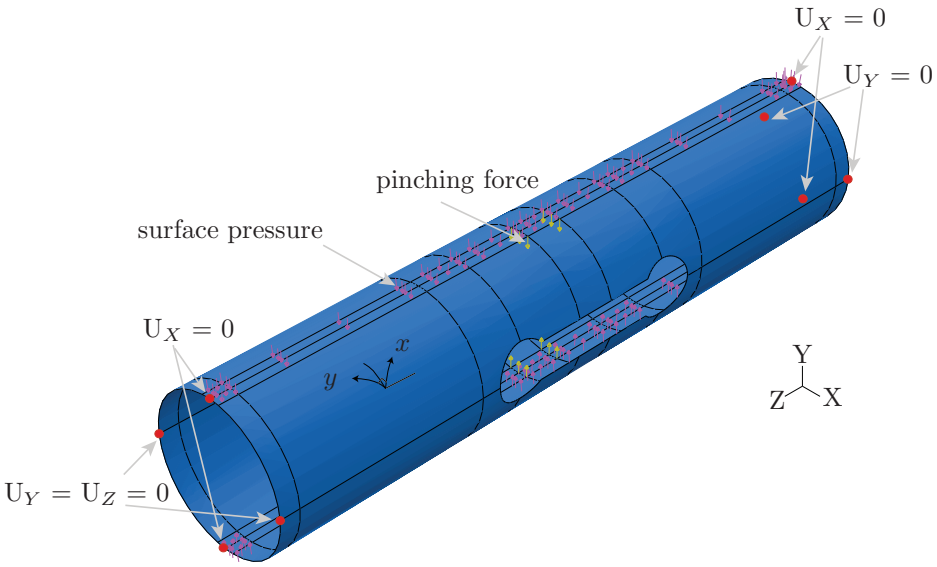

Figure 2: Finite element model.

The first stage in the folding process consists in reducing the depth of the central region of the tube hinge by applying equal and opposite "pinching" forces on six nodes on both top and bottom tape-springs, in the middle. Also the tube hinge was flattened by applying a radially inward surface pressure on 10 mm wide strips on the top and bottom of the tube hinge, Figure 2.

The material properties were obtained from a separate micro-mechanical model that determines the homogenized properties of a thin laminate.[7] This approach determines the ABD matrix in the x and y fiber directions, at 45 deg to the longitudinal and transver directions, Figure 2, and a coordinate transformation is then used to obtain the ABD matrix in a cylindrical coordinate system. This matrix is provided as an input to ABAQUS/Explicit using the command **Shell General Section*. The local coordinate system is defined by specifying a cylindrical coordinate system using the **Orientation* command.

Note that during a simulation different parts of the tube hinge come into contact with each other. This behavior is modeled by the **General contact* feature available in ABAQUS/Explicit, where the contact is defined as frictionless.

B. Folding Sequence

A folding simulation is carried out in two stages. Because a tape-spring hinge has a high bending stiffness in the fully deployed configuration, to reproduce the process of actually folding a hinge without imposing very large strains, we begin by pinching and flattening the hinge, Figures 3a and 3b. Then the hinge is folded by 180 deg by applying equal and opposite rotations on the end nodes. To minimize the accelerations anywhere in the model, the end rotations are defined as a smooth fifth-order polynomial function of time (*Smooth Step* in ABAQUS/Explicit).

Figure 3c shows the configuration of the tape-spring after imposing these rotations. Once the tube hinge is completely folded, the pinching and flattening forces are slowly removed to obtain the final fully folded configuration shown in Figure 3d. An alternative, more compact folded configuration can be obtained by removing only the pinching forces and the surface pressure applied on the bottom surface. This gives a 180 deg folded configuration with flatter ends, Figure 3e.

A small viscous pressure is applied over the external surface of the tube hinge throughout the entire folding simulation, to damp out any stress waves.[7,8] A detailed description of the simulation technique is provided in our previous papers.[5,7]

Figure 4 shows the energy variation corresponding to a folding simulation of a tube hinge with design parameters SW=10 mm, D=15 mm and L=60 mm. Note that the kinetic energy is negligibly small,

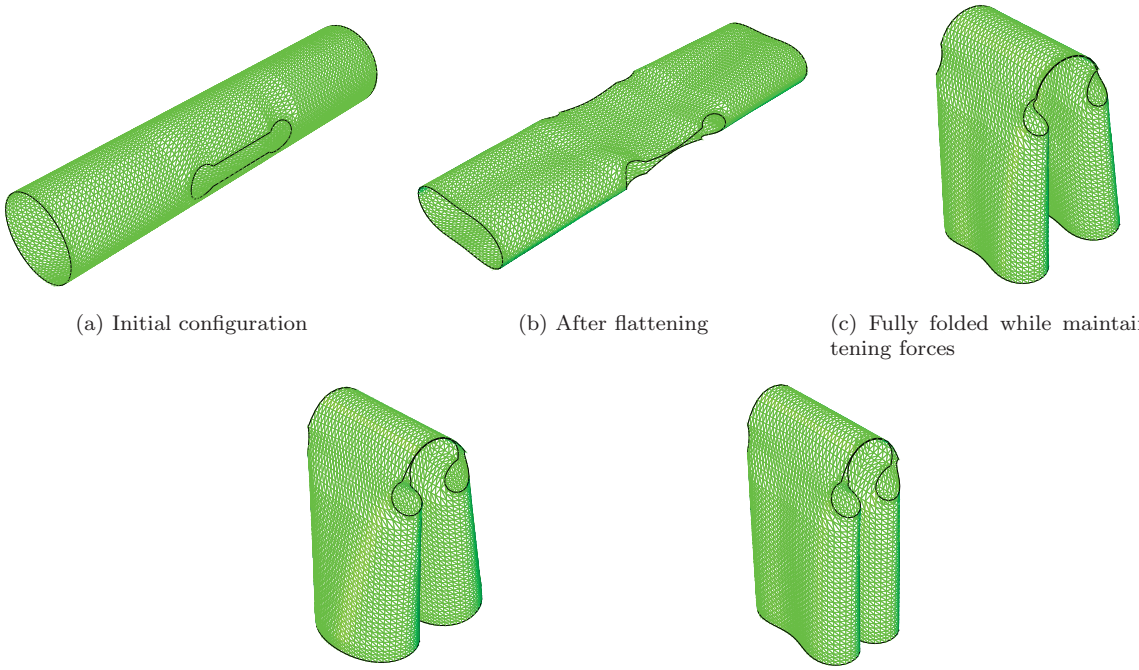

(a) Initial configuration

(b) After flattening

(c) Fully folded while maintaining flattening forces

(d) Final configuration (end rotations only)

(e) Final configuration (end-rotations and surface pressure)

Figure 3: Folding sequence.

compared to the internal energy which indicates that the response is quasi-static throughout the simulation. Also the energy balance term remains approximately zero throughout the simulation which confirms that the simulation is free of numerical instabilities.[7,9]

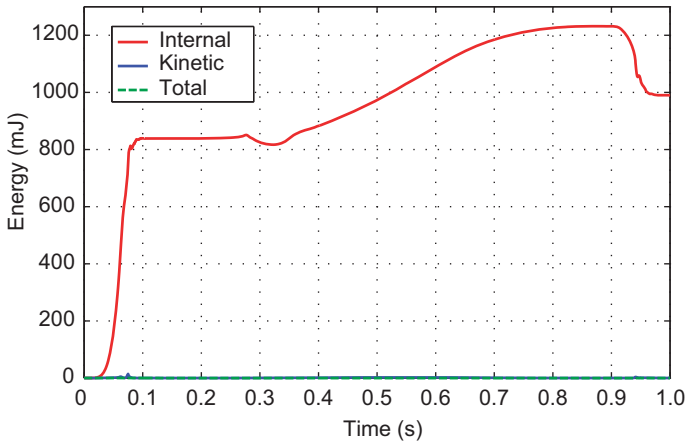

Figure 4: Energy variation during folding process (SW=10 mm, D=15 mm and L=60 mm).

III. Sensitivity to Mesh Refinement

When looking at the strain distributions obtained from a simulation it is important to check that the finite element mesh is sufficiently fine. Therefore this particular tube hinge was modeled with three different

meshes, described below.

- Mesh I : approximate element length of 3 mm, Figure 5a (2464 nodes and 2380 elements).
- Mesh II : approximate element length of 2 mm, Figure 5b (4898 nodes and 4780 elements).
- Mesh III : approximate element length of 2 mm with smaller elements near the end circles of the slots, Figure 5c (5456 nodes and elements 5304).

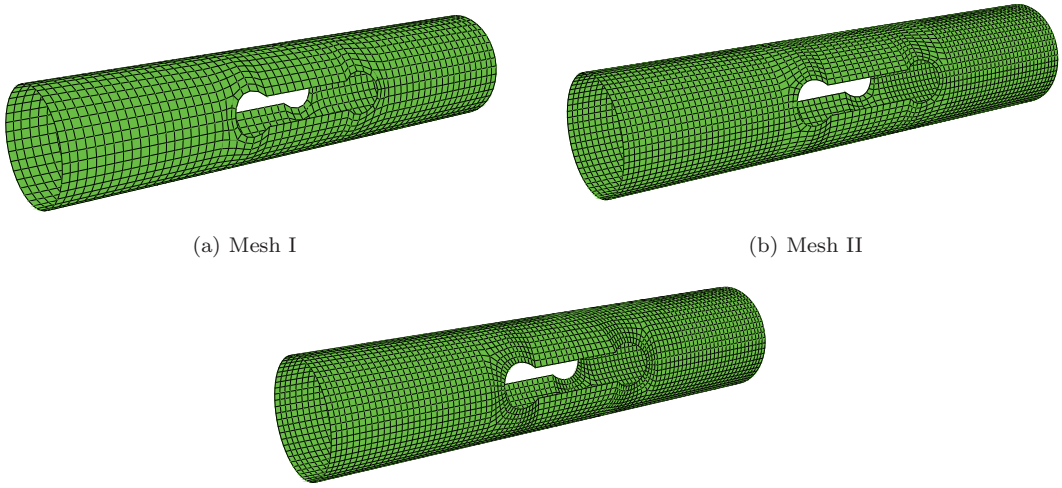

(a) Mesh I

(b) Mesh II

(c) Mesh III

Figure 5: Mesh refinement study (SW=10 mm, D=15 mm and L=60 mm).

Table 1 shows the maximum mid-surface strains ε_x, ε_y and ε_{xy} and the maximum curvatures κ_x, κ_y and κ_{xy} in the fully folded configuration, for each mesh. Here the subscripts x and y refer to the fiber directions defined in Figure 2. The analysis time listed in the last column of the table is for an Intel Core2 Quad CPU Q6600 at 2.4GHz processor machine. It should be noted that in the simulations the command **Fixed Mass Scaling, dt=1e-06, type=below min*[8] was used to artificially scale up the mass of small elements, to increase the critical time increment to 1 μs, Equation 1.

Mesh	ε_x (%)	ε_y (%)	ε_{xy} (%)	κ_x (1/mm)	κ_y (1/mm)	κ_{xy} (1/mm)	Analysis Time (h:min)
I	1.33	1.25	-1.78	0.159	0.154	-0.110	2:56
II	0.44	0.48	0.50	0.163	0.163	-0.109	5:36
III	0.51	0.45	0.51	0.186	0.186	-0.116	6:08

Table 1: Maximum mid-surface strains and curvatures for different mesh sizes.

Note that there is a significant difference in mid-surface strains between Mesh I and II whereas the values are quite similar for Mesh II and III. Considering the higher computational cost of mesh III it was decided to use Mesh II for the present study.

IV. Failure Analysis

Figures 6a to 6f show the mid-surface strain and curvature distribution in the fully folded configuration. Note that the tape spring hinge is subjected to high mid-surface strains and curvatures around the circular part of the slot, with a maximum strain of around 0.50% and a maximum curvature of 0.163 1/mm.

Considering all six mid-surface strain and curvature components we have identified the four critical locations shown in Figure 7a. These locations correspond to

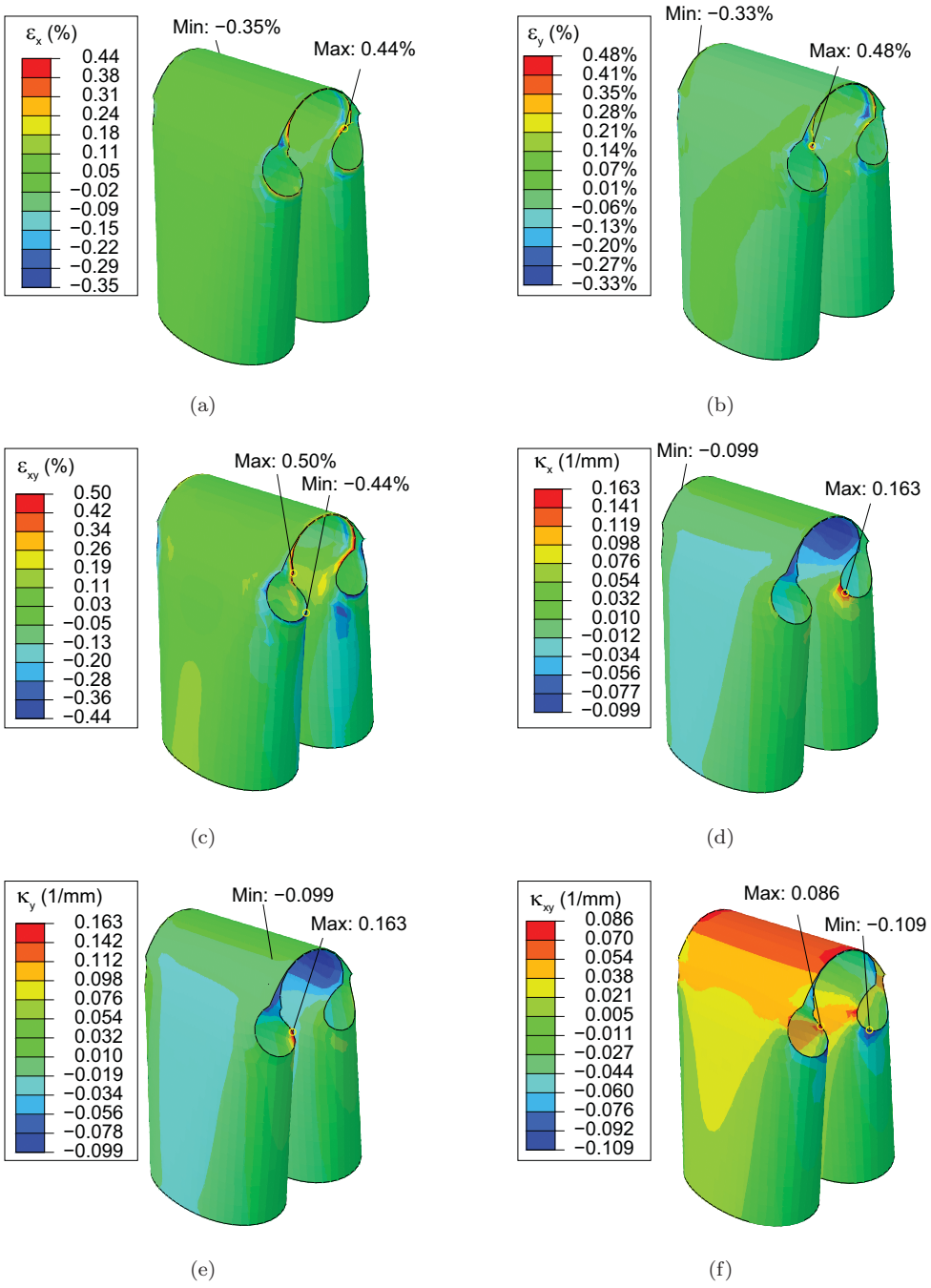

Figure 6: Mid-surface strain and curvature variation along fiber directions in fully folded configuration (SW=10 mm, D=15 mm and L=60 mm).

- Location 1: location of maximum $\varepsilon_x, \varepsilon_y$
- Location 2: location of maximum ε_{xy}
- Location 3: location of maximum κ_x, κ_y
- Location 4: location of maximum κ_{xy}

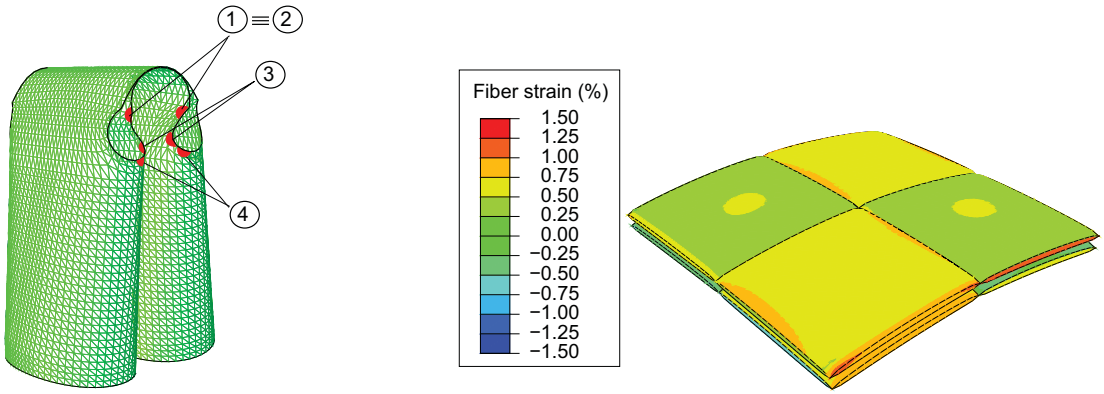

(a) Critical locations

(b) Fiber strains corresponding to location 1

Figure 7: Failure analysis (SW=10 mm, D=15 mm and L=60 mm).

At each of these locations the six mid-surface strain and curvature components were extracted from the simulation and then applied to the micro-mechanical model to obtain the maximum strains in fibers and resin.[7] Table 2 lists that values that were obtained.

Location	ε_x (%)	ε_y (%)	ε_{xy} (%)	κ_x (1/mm)	κ_y (1/mm)	κ_{xy} (1/mm)
1	0.25	0.48	0.39	-0.044	-0.039	-0.039
2	0.14	0.25	0.50	-0.040	-0.035	-0.053
3	0.14	-0.17	-0.21	0.163	0.049	-0.071
4	0.13	0.26	-0.43	0.055	0.085	-0.109

Table 2: Mid-surface strain and curvature components at four critical locations (SW=10 mm, D=15 mm and L=60 mm).

Figure 7b shows the fiber strain distribution obtained from the micro-mechanical model. Following Yang et al.,[10] the maximum fiber strain was obtained by computing the average fiber strain in a moving window with width equal to half a tow width, and then selecting the maximum average value. Similarly, the maximum resin strain was computed by computing the average transverse strain in the same moving window and then comparing the maximum average to the maximum strain in the resin filling the space between the two plies. Table 3 shows the corresponding fiber and resin strains obtained by applying the four sets of critical mid-surface strains to the micro-mechanical model. These values were compared against the ultimate tensile strains of the fibers and resin. The ultimate tensile strain of T300 fibers is 1.5%[11] and for neat Hexcel 913 resin it is 1.93%.[12] In the absence of more detailed information, this value was used without any knock-down for the presence of fibers (this is likely to be an unconservative assumption).

A detailed analysis of the the entire folding process showed that the maximum mid-surface strains were reached in the fully folded configuration. Although this result holds only for the folding sequence that was chosen, in the rest of the paper we focus only on the strains in the fully folded configuration.

Location	Maximum Strain (%)		Safety Margin (%)	
	Fiber	Resin	Fiber	Resin
1	0.92	1.27	39	34
2	0.63	0.77	58	60
3	1.36	2.38	9	fail
4	0.98	1.52	35	21

Table 3: Maximum fiber and resin strains at locations shown in Figure 7a.

V. Improved Geometries

A. Preliminary Study

Three different folding strategies were considered in this preliminary study. The first strategy was to fold the tube hinge by holding it with two elastic holders, as in our previous studies.[7] In this case the complete tube hinge was 360 mm long and it was held with two elastic rings each placed at a distance of 110 mm from the center of the hinge. The distribution of ε_x is shown in Figure 8a (note that only the 180 mm long central part is shown, for consistency with the other cases).

Next, the elastic constraints on the end cross-sections were removed as described in section B, to allow a cross-sectional distortion of the tube and so reduce the stretching of the mid-surface. The distribution of ε_x for this case is shown in Figure 8b.

Finally, a similar folding strategy was followed, but the surface pressure on the top tape spring was maintained at the end of the simulation, Figure 3e. This gives a flatter fully folded configuration and somewhat smaller strains, Figure 8c.

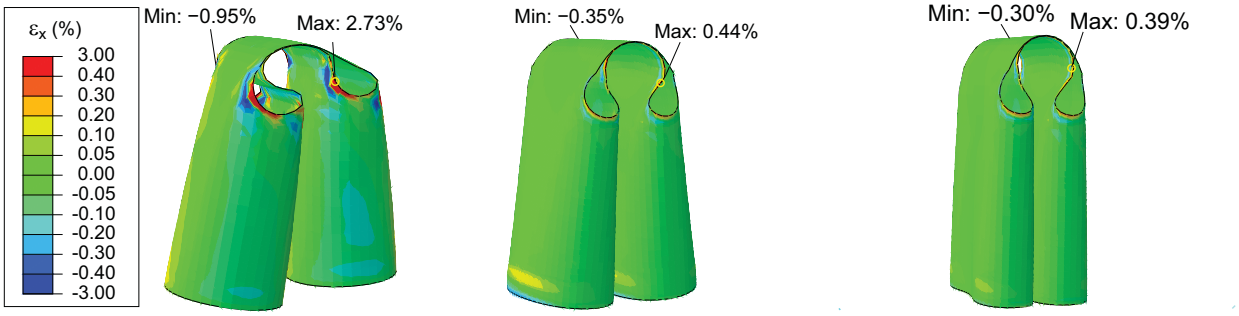

(a) With elastic holders (not shown) (b) Free (c) Flattened

Figure 8: Distribution of ε_x in the fully folded configuration with various boundary conditions (SW=10 mm, D=15 mm and L=60 mm).

Table 4 shows the maximum mid-surface strain and curvature components anywhere in each of the three cases. Note that in the case of the model with elastic holders, the mid-surface strain components are already higher than the ultimate strains of fiber and resin. Hence this particular folding strategy is not viable.

The remaining strategies lead to much lower mid-surface strains. Note that the flatter fully folded configuration has slightly lower strains, however this last configuration would add an additional parameter, the value of the normal pressure, to our sensitivity study and hence this paper will only focus on the second folding configuration.

B. Sensitivity to Slot Length

The sensitivity to L was first examined near $L = 60$ mm by exploring the range 55 mm to 70 mm at 5 mm intervals while maintaining SW=10 mm and D=15 mm. Figures 9a-9f show the ε_x distribution for each case. Only ε_x is shown for clarity. Note that strains are always higher near the slot edges and less than 0.10% everywhere else. Tables 5 presents the maximum mid-surface strain components and maximum fiber and resin strains for each design. In the case L=45 mm the maximum strain location corresponded to the

Boundary condition	ε_x (%)	ε_y (%)	ε_{xy} (%)	κ_x (1/mm)	κ_y (1/mm)	κ_{xy} (1/mm)
Elastic holders	2.73	2.92	2.62	2.474	0.270	0.173
Free	0.44	0.48	0.50	0.163	0.163	-0.109
Flattened	0.39	0.43	0.48	0.155	0.151	-0.120

Table 4: Maximum mid-surface strain and curvature components for different folding strategies.

location of highest ε_x whereas for the other cases the maximum strain location corresponded to locations of maximum κ_x or κ_y . When L=50 mm the maximum strains exceed the ultimate strains of both fiber and resin. In the cases L=45 mm and 55 mm to 70 mm the fiber strains are below the ultimate strain margin but the resin strains are higher.

Three additional values of L were considered:L=80, 85, 90 mm, Figures 9g-9i. When L=85 mm and 90 mm both fiber and resin strains are below the ultimate values and in both cases there is a safety margin of about 20% against fiber failure. However, the safety margin for the resin is only 2% and 9% in the cases L=85 mm and 90 mm respectively.

L (mm)	ε_x (%)	ε_y (%)	ε_{xy} (%)	κ_x (1/mm)	κ_y (1/mm)	κ_{xy} (1/mm)	Fiber (%)	Resin (%)
45	1.10	1.37	0.78	0.198	0.196	-0.149	1.84	2.62
50	0.75	0.78	0.83	0.200	0.194	-0.135	-2.88	-2.80
55	0.59	0.56	0.54	0.186	0.186	-0.127	1.65	2.66
60	0.44	0.48	0.50	0.163	0.163	-0.109	1.36	2.38
65	0.43	0.53	0.48	0.161	0.155	-0.097	-1.38	-2.23
70	0.44	0.45	0.55	0.150	0.151	-0.091	-1.37	-2.35
80	0.79	0.77	0.53	0.124	0.123	0.088	1.30	2.10
85	0.57	0.66	0.53	0.123	0.123	0.094	1.15	1.89
90	0.55	0.58	0.52	0.117	0.125	0.101	1.11	1.76

Table 5: Maximum mid-surface strain components and maximum fiber and resin strains for varying L ($SW = 10$ mm and $D = 15$ mm).

C. Sensitivity to Slot Width and End Circle Diameter

The next attempt was to investigate the sensitivity to SW and D to obtain a geometry with lower strains. Based on the results of Section B L=60 mm and L=90 mm were selected for further investigation.

1. L=60 mm

First we set D=15 mm and varied SW from 8 mm to 12 mm om steps of 2 mm. Figure 10 shows the variation of ε_y for the three cases and Table 6 presents the corresponding maximum mid-surface strain and curvature components and maximum fiber and resin strains. Both SW=8 mm and 12 mm exceed the ultimate strains for both fiber and resin. Hence it was concluded that SW=10 mm is best when L=60 mm and D=15 mm.

The sensitivity to D was studied by varying D from 13 mm to 17 mm while keeping SW fixed to 10 mm. Figure 11 shows the variation of ε_x and Table 7 presents the maximum mid-surface strain and curvature components and the maximum fiber and resin strains for the three cases. Note that, as already found earlier, the case D=15 mm has the lowest strains in the fully folded configuration. It is thus concluded that varying SW or D does not improve the design with L=60 mm and so a different value of L needs to be considered.

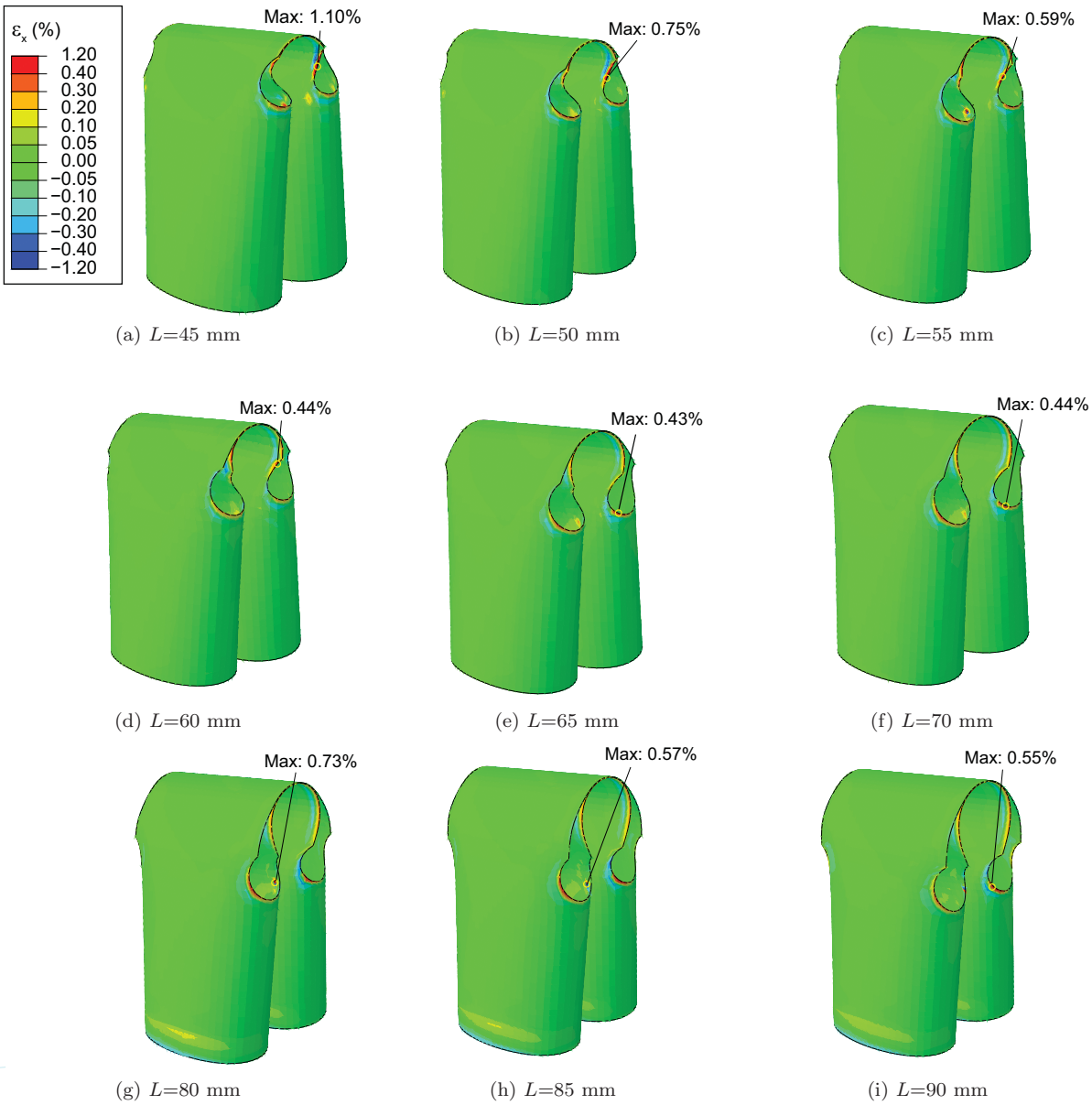

(a) L=45 mm (b) L=50 mm (c) L=55 mm

(d) L=60 mm (e) L=65 mm (f) L=70 mm

(g) L=80 mm (h) L=85 mm (i) L=90 mm

Figure 9: Distribution of ε_x in the fully folded configuration with varying L (SW=10 mm and D=15 mm).

SW (mm)	ε_x (%)	ε_y (%)	ε_{xy} (%)	κ_x (1/mm)	κ_y (1/mm)	κ_{xy} (1/mm)	Fiber (%)	Resin (%)
8	0.75	0.81	0.62	0.177	0.175	-0.112	-1.58	-2.57
10	0.44	0.48	0.50	0.163	0.163	-0.109	1.36	2.38
12	0.47	0.78	0.56	0.180	0.155	-0.111	-1.61	-2.59

Table 6: Maximum mid-surface strain and curvature components and maximum fiber and resin strains for varying SW ($D = 15$ mm and $L = 60$ mm).

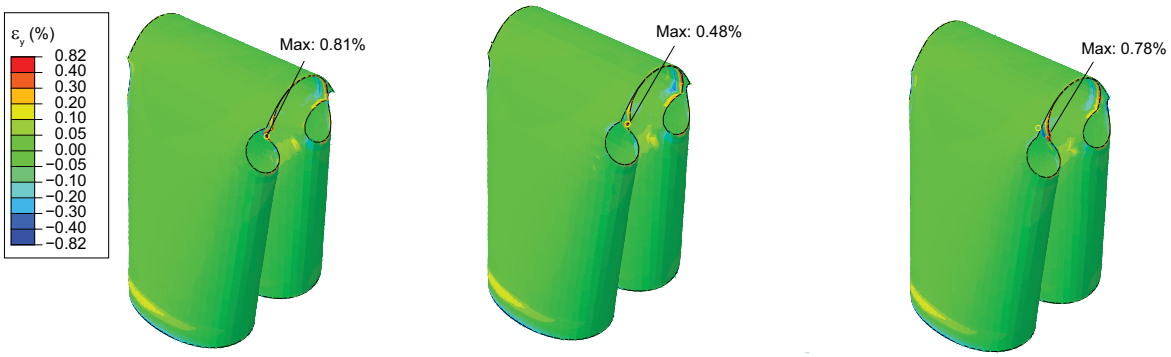

(a) SW=8 mm (b) SW=10 mm (c) SW=12 mm

Figure 10: Distribution of ε_y in fully folded configuration for varying SW (D=15 mm and L=60 mm).

(a) D=13 mm (b) D=15 mm (c) D=17 mm

Figure 11: Distribution of ε_x in the fully folded configuration for varying D (SW=10 mm and L=60 mm).

D (mm)	ε_x (%)	ε_y (%)	ε_{xy} (%)	κ_x (1/mm)	κ_y (1/mm)	κ_{xy} (1/mm)	Fiber (%)	Resin (%)
13	1.12	0.86	0.57	0.174	0.185	-0.123	-1.60	-2.61
15	0.44	0.48	0.50	0.163	0.163	-0.109	1.36	2.38
17	0.92	0.96	0.68	0.163	0.161	-0.103	1.47	2.37

Table 7: Maximum mid-surface strain components and maximum fiber and resin strains for varying D (SW = 10 mm and L = 60 mm).

2. Sensitivity at L=90 mm

Section V.B had shown that the design with L=90 mm, SW=10 mm and D=15 mm can be folded safely. To obtain a design with a better safety margin we varied SW from 8 mm to 12 mm while maintaining the ratio SW/D at either 1/2, 2/3 or 1. Table 8 presents the maximum mid-surface strain and curvature component and the maximum fiber and resin strains for each case. Note that when SW/D =1, both fiber and resin strains exceed the ultimate limit, but having an end circle with a diameter D larger than SW reduces the maximum strain in the folded structure. Note that our previous design had SW/D=1.

L (mm)	SW (mm)	D (mm)	$\approx SW/D$	ε_x (%)	ε_y (%)	ε_{xy} (%)	κ_x (1/mm)	κ_y (1/mm)	κ_{xy} (1/mm)	Fiber (%)	Resin (%)
90	8	15	1/2	0.52	0.51	0.51	0.117	0.114	0.112	1.05	1.68
90	10	10	1	1.21	1.18	1.05	-0.079	-0.079	0.147	1.72	2.32
90	10	15	2/3	0.55	0.58	0.52	0.117	0.125	0.101	1.11	1.76
90	12	12	1	0.76	0.91	0.81	0.081	0.081	0.110	1.59	2.41
90	12	18	2/3	0.65	0.63	-0.81	0.111	0.111	0.083	-0.92	-1.65
90	12	24	1/2	0.57	0.57	0.55	0.122	0.121	0.098	-1.09	-1.77

Table 8: Maximum mid-surface strain components and maximum fiber and resin strain for varying SW and D (L=90 mm).

In all cases with SW/D=1/2 or 2/3 the fiber strains have decreased and have a safety margin higher than 23%. In the cases SW=8 mm, D=15 mm and SW=12 mm, D=18 mm the resin strains have decreased from 1.76% to 1.68% and 1.65% respectively. This gives an approximate safety margin of 13% against resin failure.

Although the design with SW=12 mm and D=18 mm has the lowest strain than any other design that has been considered, the design SW=8 mm and D=15 mm removes the least amount of material from the original tube. For this reason, the design with L=90 mm, SW=8 mm and D=15 mm is considered as the best design obtained from the present study.

VI. Further Analysis of Optimized Design

A 220 mm long (chosen to match the center to center distance of the experimental rig used in Ref[7]) fully deployed tube with the selected slot design (SW=8 mm, D=15 mm and L=90 mm) was analyzed to determine its properties. Its fundamental natural frequency is 220 Hz, its axial stiffness 1081 N/mm and its torsional stiffness 576 Nmm/deg.

Figure 12 shows the moment rotation behavior of this particular tape-spring hinge design. This relationship was obtained by rotating the hinge from the fully folded configuration to its initial, unstressed configuration while applying pure bending constraints. The viscous pressure coefficient was set at $c_v = 2 \times 10^{-5}\ \rho c_d$.[7]

Starting from the fully folded configuration, this moment-rotation relationship consists of four main parts, as follows. A linear portion with small slope, from 170 deg to 95 deg and moment decreasing from 168 Nmm to 136 Nmm. An oscillating response around a mean of 140 Nmm, from 95 deg to 45 deg, when the symmetric fold gradually moves to an asymmetric configuration. A slowly rising portion with the moment rising smoothly to 677 Nmm with three clear peaks. The first peak is due to snapping of the top tape-spring. The second is due to an oscillation of the bottom tape-spring due to the dynamic snapping of the top tape-spring. The third and highest peak occurs when the entire hinge is fully latched. A linear potion with a high gradient as the latched hinge unloads to its unstressed configuration.

In order to obtained a less noisy response, the viscous pressure load over the external surface of the whole tube hinge was increased by a factor of 5, after carrying out a sensitivity study similar to that presented in Ref.[7] The corresponding moment-rotation relationship is shown in Figure 13. Note that now the only vibration is near the highest peak which is actually a dynamic event.

The new response shows significant deviation from the response with low viscous pressure. It changes its configuration from symmetric to asymmetric at an angle of 157 deg, instead of around 90 deg previously. This sudden change occurs with a small peak moment of 190 Nmm at an angle 155 deg. Then it follows a

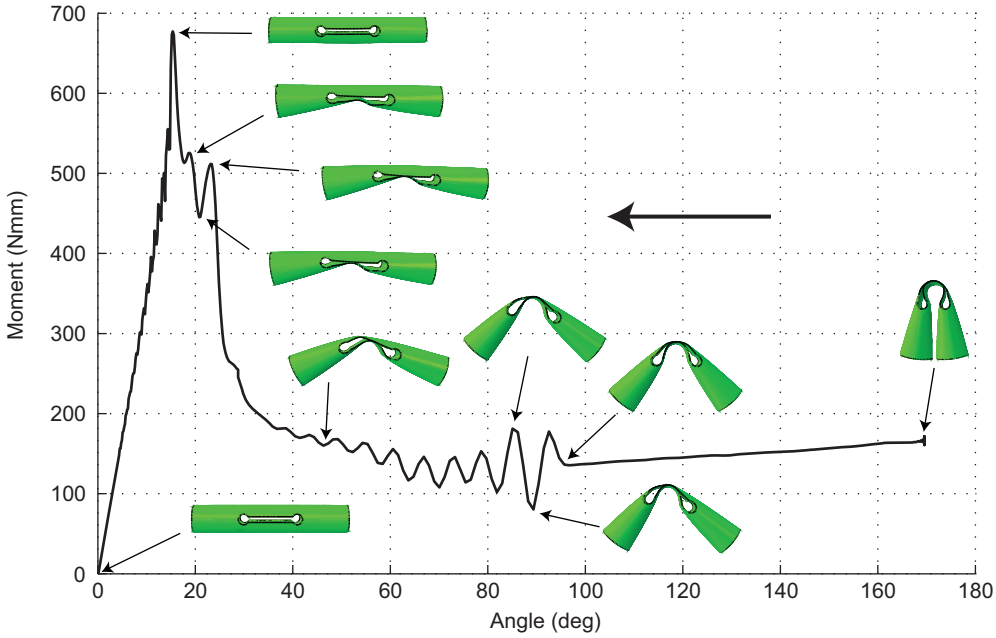

Figure 12: Deployment moment-rotation relation for optimized design ($c_v = 2 \times 10^{-5}\ \rho c_d$).

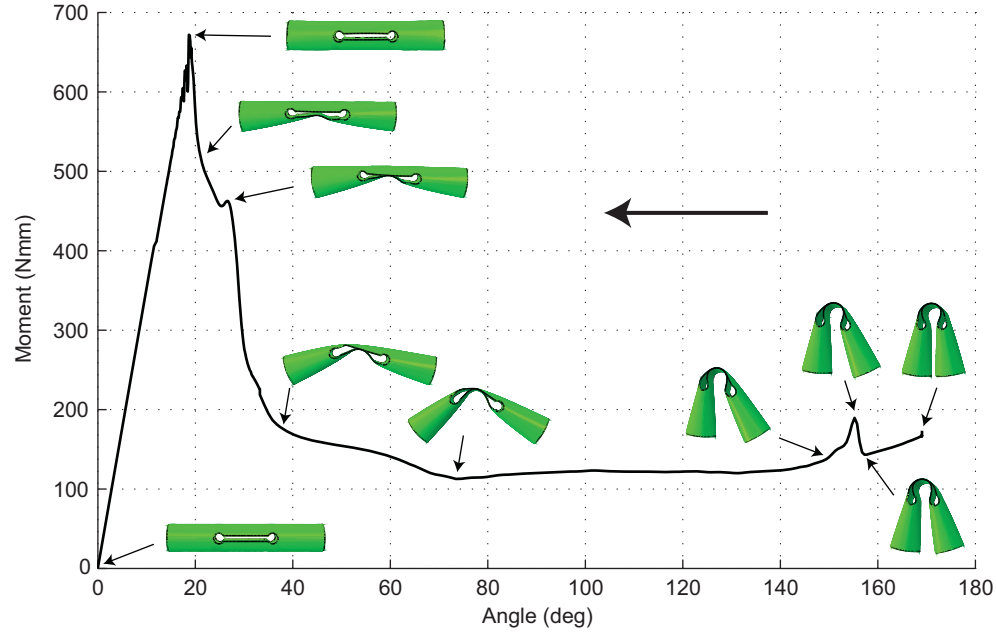

Figure 13: Deployment moment-rotation relation for optimized design ($c_v = 10 \times 10^{-5}\ \rho c_d$).

fairly smooth curve, varying from 150 Nmm to 112 Nmm. From 70 deg the top tape-spring starts becoming straight and this leads to a rise in the moment. A secondary peak of 463 Nmm at 27 deg corresponds to latching of the top tape-spring. Finally the complete hinge latches at an angle of 19 deg with a peak of 672 Nmm and then achieves its unstressed configuration.

Note that both responses show a similar peak corresponding to dynamic snapping of the tube hinge.

VII. Experimental Observations

To validate the failure analysis results obtained in Section V, two designs were selected and physical models were constructed to check their folding behavior. The first attempt was to select a failure critical design and check whether it actually fails. Based on the sensitivity analysis carried in Section C a tube hinge with SW=10 mm, D=15 mm and L=60 mm tube hinge was constructed. This tape-spring hinge was flattened by about 50% and then it was carefully folded, however the hinge cracked near the circular edges, Figure 14, as predicted. The experiment was repeated on an identical tape-spring hinge with the same parameters to make sure that the failure had not been due to manufacturing defects. This new hinge cracked in the same regions as the previous one.

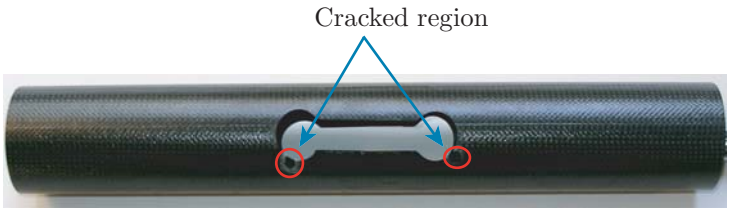

Figure 14: Tube hinge of SW=10 mm, D=15 mm and L=60 mm.

Our second choice was to construct the improved design selected in Section VI. This tape-spring hinge was carefully folded, first by flattening it and then by rotating the ends. The tube hinge cross-section was allowed to deform freely during the folding process. Figure 15a and 15b show the undeformed and fully folded configurations, respectively, of this optimized design. Note that the two ends of the tube take a conical configuration to reduce strains near the slot edges.

(a) Deployed configuration

(b) Fully folded configuration

Figure 15: Tube hinge with SW=8 mm, D=15 mm and L=90 mm.

VIII. Comparison with Old Design

In our previous studies[5–7] we considered a tube hinge consisting of two tape-springs separated by slots with $SW = D = 30$ mm and $L = 140$ mm. The main concerns with this design were its torsional stiffness and the fact that the the folds could move along the individual tape springs and so the hinge folded asymmetrically.

The new design has much wider and shorter tape-springs which increases the torsional stiffness by six times, the axial stiffness by a factor of two and the bending stiffness by one third, Table 9. Note that all these values are given for a 220 mm long tube hinge. The fully folded new tube hinge stores almost two and a half times more strain energy than the old hinge which would be an advantage for deploying large structures. Also the new design has a much higher peak moment during deployment and it can also be expected that the locking moment, i.e. the moment that needs to be applied to start folding the hinge, will also be much higher.

Note that the peak moment of 320 Nmm for the old design is much lower than the value obtained in Ref.[7] because here the end cross-sections were not constrained with elastic holders. Figure 16 compares the moment-rotation relationships of old and new designs, both obtained with $c_v = 10 \times 10^{-5}\ \rho c_d$. The old design has a steady state moment of around 65 Nmm with a single peak of 320 Nmm at an angle of 9 deg. As described in Section VI the new hinge has a steady state moment of around 130 Nmm with two peaks of 463 Nmm and 672 Nmm at angles 27 deg and 19 deg, corresponding to the latching of each tape-spring. Note that near the origin the two designs appear to have the same slope, which would indicate that they have the same bending stiffness. However the stiffness values described above were obtained with slightly different boundary conditions, more representative of the connections in an actual application.

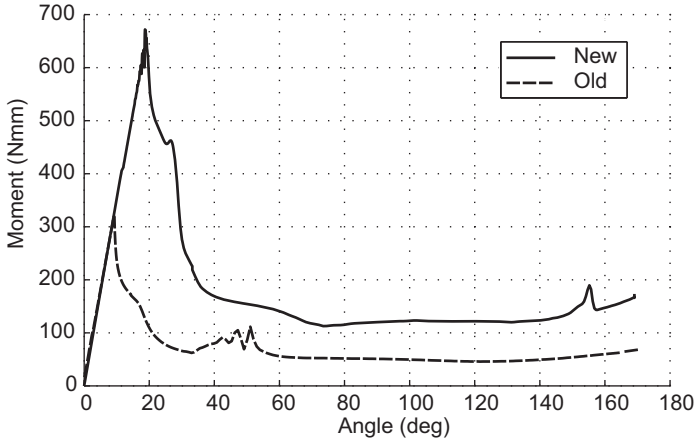

Figure 16: Comparison of moment-rotation variation for previous and optimized designs.

Design	L (mm)	Tape-spring width (mm)	Axial stiffness (N/mm)	Bending stiffness (Nmm/deg)	Torsional stiffness (Nmm/deg)	Stored energy (mJ)	Peak moment (Nmm)
Old	140	25.5	562	3305	97	306	320
New	90	56	1081	4330	576	742	672

Table 9: Comparison of previous and optimized designs.

IX. Conclusions

This paper has improved the design considered in Refs.[5–7] The sensitivity of the maximum strain, averaged over a half tow width to estimate the safety margin against fiber and resin failure, to three parameters L, SW and D safe design was investigated and then experimentally validated. The shortest slot length that

was considered in detail had $L = 60$ mm but for this case no values of the parameters were found that would reduce the maximum strains to acceptable levels.

A new design with $L = 90$ mm was obtained, which has a six times increase in torsional stiffness, twice the axial stiffness, a one third increase in bending stiffness and almost two and a half times the stored energy of the original design. The shorter tape-springs provide better control over the position of the folded region in the hinge and hence the kinematics of deployment are likely to be better constrained. Further investigation of this design may well lead to alternative slot configurations with even shorter L.

One of the significant findings of this paper is that shorter hinges can be obtained if one allows the end cross-sections to deform freely. This means that it is important to understand how the hinge is going to be connected to the spacecraft and to the structure to be deployed by the hinge. It has also been found that flattening the hinge in the fully folded configuration, Figure 3b, further reduces the strains in the structure. However, this effect was not studied in depth in the present paper.

The optimization study that has been carried out has targeted a hinge that could be folded 180 deg without breaking, with minimum removal of material from the original tube. Only quasi-static folding and deployment have been considered and obviously the effects of dynamic deployment will need to be considered in future studies.

Acknowledgments

We thank Dr Michael Sutcliffe for helpful discussions and John Ellis (Hexcel, UK) for providing materials. HM thanks the Cambridge Commonwealth Trust and the California Institute of Technology for financial support.

References

[1]Adams, D.S. and Mobrem, M. (2009) "Lenticular Jointed Antenna Deployment Anomaly and Resolution Onboad the Mars Express Spcaecraft," *Journal of Spacecraft and Rockets*, Vol. 46, No. 2, pp. 403-410.

[2]Boesch, C., Pereira, C., John, R., Schmidt, T., Seifart, K., Sparr, H., Lautier, J.M., Pyttel, T. (2008) "Ultra Light Self-Motorized Mechanism for Deployment of Light Weight Space Craft Appendages," *39th Proceedings of Aerospace Mechanisms Symposium*, 7-9 May 2008, Newport, NASA Marshall Space Flight Center.

[3]Sickinger, C., Herbeck, L., Strohelin, T., Torrez-Torres, J. (2004) "Lightweight Deployable Booms: Design, Manufacture, Verification, and Smart Materials Application," *55th International Astronautical Congress, IAF/IAA/IISL*, October 04 - 08 2004, Vancouver, Canada.

[4]Yee, J. C. H., and Pellegrino, S. (2005) Composite tube hinges, *Journal of Aerospace Engineering*, Vol. 18, 224-231.

[5]Mallikarachchi, H.M.Y.C. and Pellegrino, S. (2008) "Simulation of Quasi-Static Folding and Deployment of Ultra- Thin Composite Structures," *49th AIAA/ASME/ASCE/AHS/ASC Structures, Structural Dynamics, and Materials Conference*, AIAA-2008-2053, Schaumburg, Illinois, 07-10 April 2008.

[6]Mallikarachchi, H.M.Y.C. and Pellegrino, S. (2009) "Deployment Dynamics of Composite Booms with Integral Slotted Hinges," *50th AIAA/ASME/ASCE/AHS/ASC Structures, Structural Dynamics, and Materials Conference*, AIAA-2009-2631, Palm Springs, California, 4 - 7 May.

[7]Mallikarachchi, H.M.Y.C. and Pellegrino, S. (2009) "Quasi- Static Folding and Deployment of Ultra-Thin Composite Structures," submitted for publication.

[8]SIMULIA, ABAQUS/Explicit Version 6.8, Providence, RI.

[9]Belytschko, T., Liu, W.K. and Moran, B. (2000) "6.2.3 Energy balance," *Nonlinear Finite Elements for Continua and Structures,* Chichester, J. Wiley & Sons. , pp. 315-316.

[10]Yang, Q.D., Rugg, K.L., Cox, B.N., Marshall, D.B. (2005) "Evaluation of Macroscopic and Local Strains in a Three-Dimensional Woven C/SiC Composite," *Journal of the American Ceramic Society*, Vol. 88, No. 3, pp. 719-725.

[11]Torayca. Technical Data Sheet No. CFA-001, T300 Data Sheet.

[12]Hexcel Corporation, *Technical Data Sheet HexPly913*, 2007.